

# **Oxidative stress-mediated PANoptosis and ferroptosis: Exploration of multimodal cell death triggered by an AIE-active nano-photosensitizer via photodynamic therapy**

Yuqing Wang<sup>1#</sup>, Chuxing Chai<sup>2#</sup>, Wangxing Lin<sup>3#</sup>, Juanmei Cao<sup>1,4</sup>, Zhuoxia Li<sup>2</sup>, Yifan Jin<sup>1</sup>, Yiting Xu<sup>5</sup>, Jianyu Zhang<sup>6</sup>, Yong Qu<sup>2</sup>, Jinshan Zhan<sup>1</sup>, Tianqi Zhao<sup>1</sup>, Yufan Chen<sup>1</sup>, Meng Gao<sup>3\*</sup>, Changzheng Huang<sup>1\*</sup>, Min Li<sup>2\*</sup>

1. Department of Dermatology, Union Hospital, Tongji Medical College, Huazhong University of Science and Technology, Wuhan 430022, China.
2. Department of Hepatobiliary Surgery, Union Hospital, Tongji Medical College, Huazhong University of Science and Technology, Wuhan 430022, China.
3. National Engineering Research Center for Tissue Restoration and Reconstruction, Key Laboratory of Biomedical Engineering of Guangdong Province, Key Laboratory of Biomedical Materials and Engineering of the Ministry of Education, Innovation Center for Tissue Restoration and Reconstruction, School of Materials Science and Engineering, South China University of Technology, Guangzhou 510006, China.
4. Department of Dermatology, First Affiliated Hospital, Shihezi University, Shihezi 832008, China.
5. Central Laboratory, Union Hospital, Tongji Medical College, Huazhong University of Science and Technology, Wuhan 430022, China.
6. Department of Chemistry, Hong Kong Branch of Chinese National Engineering Research Center for Tissue Restoration and Reconstruction, The Hong Kong University of Science and Technology, Hong Kong 999077, China.

<sup>#</sup>These authors equally contributed to this work.

<sup>\*</sup>Corresponding authors:

Prof. Min Li, M.D., Ph.D., Department of Hepatobiliary Surgery, Union Hospital, Tongji Medical College, Huazhong University of Science and Technology, Wuhan 430022, China. Email: liminmed@hust.edu.cn.

Prof. Changzheng Huang, M.D., Ph.D., Department of Dermatology, Union Hospital, Tongji Medical College, Huazhong University of Science and Technology, Wuhan 430022, China. Email: hcz0501@126.com.

Prof. Meng Gao, Ph.D., National Engineering Research Center for Tissue Restoration and Reconstruction, Key Laboratory of Biomedical Engineering of Guangdong Province, Key

Laboratory of Biomedical Materials and Engineering of the Ministry of Education, Innovation Center for Tissue Restoration and Reconstruction, School of Materials Science and Engineering, South China University of Technology, Guangzhou 510006, China. Email: msmgao@scut.edu.cn.

## **Abstract**

**Background:** Aggregation-induced emission (AIE)-based photodynamic therapy (PDT) represents a promising strategy for cancer treatment for its capacity to activate specific cell death pathways through pronounced oxidative stress. While the activation of specific death pathways has been correlated with PDT efficiency and overall effect, the systematic coordination of oxidative stress across different cell death modalities to amplify therapeutic effects remains unexplored. Current research lacks systematic investigation into how oxidative stress coordinates multiple cell death pathways to amplify therapeutic outcomes of PDT.

**Methods:** We developed an AIE-based nano-photosensitizer (T-T NPs) to induce multimodal cell death through PDT. The system was characterized for mitochondrial targeting capability and reactive oxygen species (ROS) generation. Mechanistic analyses were conducted to evaluate programmed cell death pathways and ferroptosis induction in tumor.

**Results:** T-T NPs exhibited superior mitochondrial targeting and highly efficient ROS generation. This dual effect successfully triggered PANoptosis and ferroptosis. The synergistic activation of these pathways significantly enhanced PDT-mediated antitumor efficacy.

**Conclusion:** Our findings reveal that AIE-driven PDT can orchestrate multimodal cell death in tumor through oxidative stress modulation. By concurrently activating PANoptosis and ferroptosis, this approach establishes a novel paradigm for overcoming limitations of conventional single-pathway targeted PDT.

**Key words:** Photodynamic therapy; Aggregation-induced emission; Oxidative stress; PANoptosis, Ferroptosis

**Conflict of Interest:** The authors declare no conflict of interest.

**Acknowledgements:** This work was supported by the National Natural Science Foundation of China (82172754, 22475073, 22175065, 81972565). The Scheme 1(III) was Created in BioRender. Chai, C. (2024) <https://BioRender.com/i13y151>. The Scheme 1(I) and (II), Figures 1A, 1B, 5A, 6A were

drawn by Figdraw (<https://www.figdraw.com/#/>).

**Data Availability Statement:** The data that support the findings of this study are available in the supplementary material of this article.

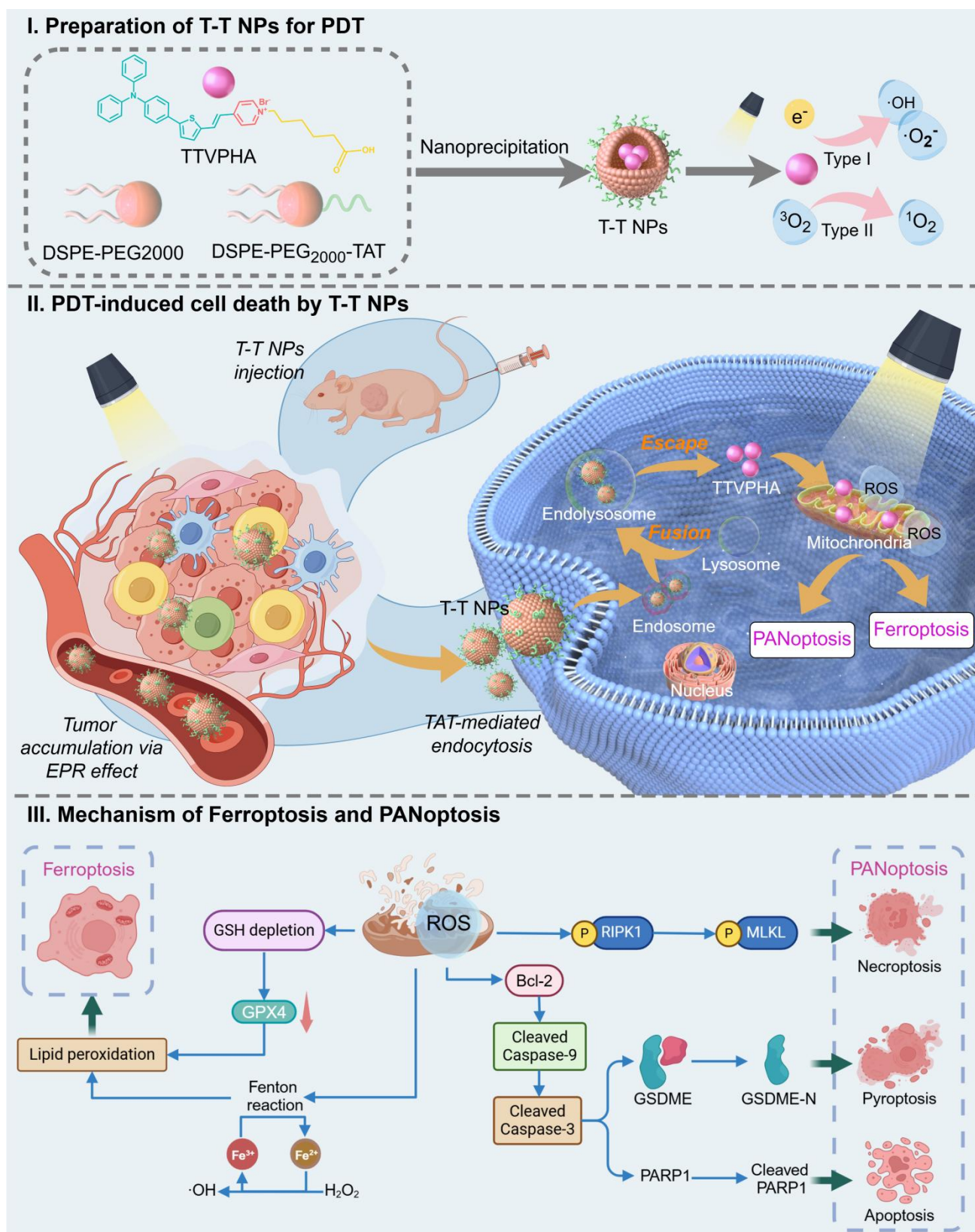
## Introduction

Photodynamic therapy (PDT) has emerged as a promising cancer treatment modality due to its non-invasive nature and minimal side effects. As a localized treatment, PDT has been applied to a wide range of tumors, including superficial skin tumors, head and neck cancers, esophageal cancer, extrahepatic cholangiocarcinoma, lung cancer, and bladder cancer, demonstrating considerable clinical potential [1-6]. PDT operates by activating photosensitizers (PSs) with light at specific wavelengths, leading to the production of reactive oxygen species (ROS) and inducing oxidative stress, which damages cellular components and ultimately causes cell death [7-8]. To enhance PDT efficacy, various novel PSs have been developed. Recently, PSs with aggregation-induced emission (AIE) properties have attracted significant attention due to their enhanced photostability and increased ROS generation, leading to greater tumor suppression compared to traditional PSs with aggregation-caused quenching (ACQ) effects [9-13].

The core antitumor mechanism of PDT involves the generation of ROS, causing oxidative stress and subsequent cell death [14]. Various cell death mechanisms, such as apoptosis and necrosis, are closely tied to oxidative stress induced by PDT [15-16]. More recently, novel cell death pathways like pyroptosis and ferroptosis have been observed in cancer cells undergoing PDT-induced oxidative stress [17-18]. These unique forms of cell death can elicit strong immunogenic responses, thereby enhancing PDT's antitumor efficacy [19]. For instance, Wang et al. [20] designed a membrane-targeted AIE-based PS, TBD-3C, which effectively induced pyroptosis and stimulated cancer immunotherapy through PDT. Similarly, Fang et al. [21] developed a multifunctional PS (CNTPA-TPA) that triggered ferroptosis and immune activation, leading to enhanced antitumor effects. Given the influence of cell death modalities on PDT's anticancer efficacy, strategies have emerged that combining PDT with cell death inducers, such as erastin (ferroptosis inducer) [22], decitabine (pyroptosis inducer) [23], and copper ions (cuproptosis inducer) [24], within a single nano-delivery system to activate specific cell death mechanisms. Most studies have examined the

independent effects of these death pathways in PDT; however, recent research suggests that these pathways may interact synergistically, potentially amplifying antitumor effects. Initial studies have begun exploring dual cell death modalities, such as apoptosis-ferroptosis [25-26] and pyroptosis-ferroptosis [27]. Our preliminary findings also intimate that cell death pathways may form a complex multimodal network in PDT, collaboratively enhancing antitumor efficacy [28]. Based on these observations, we hypothesize that PDT can activate a multimodal cell death network through oxidative stress, achieving amplified antitumor outcomes and guiding the design of new PSs.

In this study, we developed a novel nano-formulated PS, T-T NPs, by encapsulating the mitochondria-targeted AIE-based PS TTVPHA within DSPE-PEG<sub>2000</sub> and functionalizing it with TAT (a cell-penetrating peptide) to enhance cellular uptake. In both *in vitro* and *in vivo* models, we demonstrated that T-T NPs-mediated PDT produces substantial ROS in tumor cells, activating key factors involved in multiple cell death pathways, including PANoptosis (pyroptosis, apoptosis, and necroptosis) and ferroptosis across various cancers (melanoma and hepatocellular carcinoma), as illustrated in **Scheme 1**. To our knowledge, this study is the first to reveal that AIE PS-mediated PDT can trigger a complex network of multimodal cell death involving PANoptosis and ferroptosis, providing mutual reinforcement for enhanced antitumor effects. This multimodal strategy may offer a more comprehensive approach to cancer treatment with PDT, potentially overcoming resistance mechanisms, enhancing therapeutic efficacy, and simplifying the nanoformulation design for PSs.



**Scheme 1.** Schematic illustration of (I) preparation process and PDT pathway of T-T NPs; (II) tumor accumulation, cancer cell endocytosis, and cell death modalities of T-T NPs-mediated PDT; (III) mechanisms of ROS-induced multimodal cell death network through PDT of T-T NPs.

## 1. Preparation and characterization of T-T NPs

Mitochondria, central to cellular processes like energy metabolism, calcium homeostasis, and cell death regulation, are critical targets in organelle-focused cancer therapy. Mitochondria-targeted AIE PSs offer significant potential to enhance PDT efficacy by promoting cancer cell death and improving overall anticancer effects [29]. As shown in **Figure 1A**, **Figure S1**, the mitochondria-targeted AIE probe TTVPHA, synthesized with a D- $\pi$ -A scaffold as previously reported, was constructed from 1-(5-Carboxypentyl)-4-methylpyridin-1-ium bromide and 5-(4-(diphenylamino)phenyl)thiophene-2-carbaldehyde, known for its photosensitive property [30]. TTVPHA was then encapsulated into nanoparticles (NPs) using DSPE-PEG<sub>2000</sub> and DSPE-PEG<sub>2000</sub>-TAT via a nanoprecipitation process (**Figure 1B**). The TAT peptide on the NPs surface significantly enhances the cellular uptake of T-T NPs [31-34].

The absorption and emission spectra of T-T NPs in aqueous solution show a maximum absorption at 464 nm and emission at 654 nm (**Figure 1C**). Dynamic light scattering (DLS) measurements and transmission electron microscopy (TEM) imaging (**Figure 1D**) confirmed that T-T NPs formed stable nanoparticles in water with a diameter of approximately 167.9 nm and a Zeta potential of -21.7 mV. ROS generation was assessed using commercial indicators. Specifically, the total ROS produced by T-T NPs under light exposure was quantified using 2',7'-dichlorodihydrofluorescein (DCFH) (**Figures 1E**, **Figure S2A**). To identify specific ROS types, dihydrorhodamine 123 (DHR123), hydroxyphenyl fluorescein (HPF), and singlet oxygen sensor green (ABDA) were used to detect O<sub>2</sub><sup>-</sup>, •OH, and <sup>1</sup>O<sub>2</sub>, respectively. Under white light exposure, DHR123 and HPF fluorescence intensities increased (**Figures 1F-G**, **Figure S2B-C**), while ABDA absorbance decreased (**Figures 1H**), indicating that T-T NPs generate significant amounts of O<sub>2</sub><sup>-</sup> and •OH, with minimal <sup>1</sup>O<sub>2</sub> production.

To understand the photophysical properties of T-T NPs, density functional theory (DFT) and time-dependent DFT (TD-DFT) calculations were performed. The HOMO electron clouds primarily reside on the electron-rich triphenylamine-thiophene unit, with slight delocalization on the vinyl unit, while the LUMO is primarily localized on the pyridinium moiety. This illustrates a large HOMO-LUMO orbital separation and typical donor-acceptor characteristics [35]. As shown in **Figure 1I**, the HOMO-LUMO separation facilitates intersystem crossing (ISC) by reducing the  $\Delta E_{ST}$  value, with energy gaps  $\Delta E_{S1-T2}$  and  $\Delta E_{S1-T1}$  calculated at -0.190 eV and 1.302 eV, respectively. The

smaller S<sub>1</sub>-T<sub>2</sub> energy gap suggests an efficient ISC from S<sub>1</sub> to T<sub>2</sub>, with internal conversion from T<sub>2</sub> to T<sub>1</sub> further supporting ROS generation. Additionally, the triplet-ground state energy gap ( $\Delta E_{T_1-S_0}$ ) of TTVPHA was calculated to be 0.899 eV, lower than the <sup>3</sup>O<sub>2</sub> and <sup>1</sup>O<sub>2</sub> energy gap (1.61 eV), indicating that T-T NPs are efficient in generating type I ROS (O<sub>2</sub><sup>•-</sup> and •OH) (**Figure 1J**). These results demonstrate that T-T NPs can generate ROS through both type I and type II photosensitized oxidation, which is advantageous for PDT in hypoxic tumors by mitigating oxygen depletion during treatment.

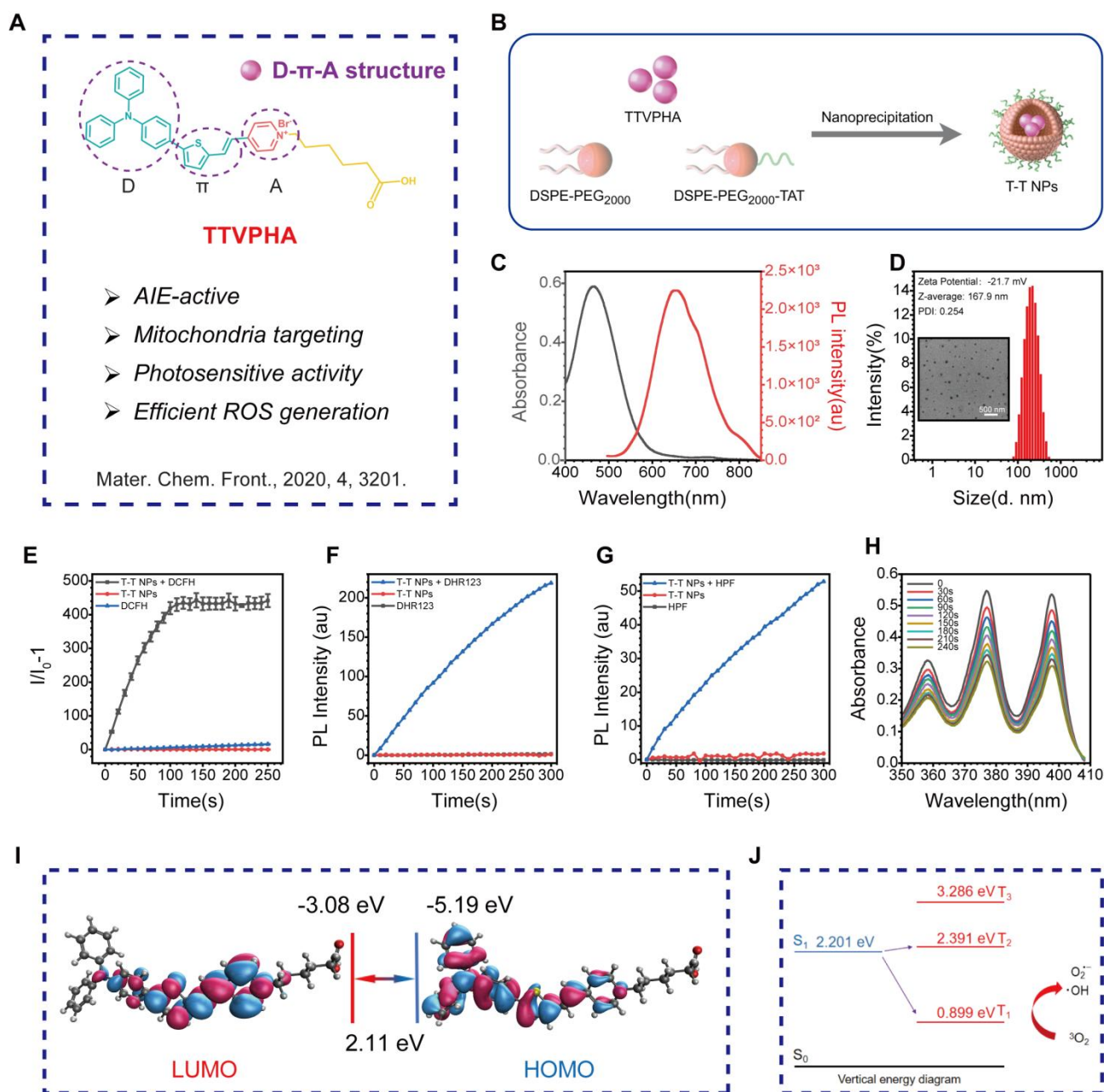


**Figure 1. Preparation and physicochemical characterizations of T-T NPs. (A)** The chemical structure of



AIE-active PS TTVPHA. **(B)** Schematic illustration of T-T NPs preparation. **(C)** The corresponding UV/Vis absorption spectra and fluorescence spectra of T-T NPs. **(D)** Size distributions and Zeta potential of T-T NPs were measured by DLS, and TEM image of T-T NPs. **(E-H)** The total ROS generation of T-T NPs in aqueous solution measured by the emission intensity of DCFH (10  $\mu$ M), DHR123 (10  $\mu$ M) and HPF (10  $\mu$ M) at 530 nm, and ABDA (50  $\mu$ M) at 350~410 nm after white light irradiation (20 mW·cm<sup>-2</sup>), to detect O<sub>2</sub><sup>•-</sup>, •OH and <sup>1</sup>O<sub>2</sub> generation, respectively. **(I)** HOMO and LUMO distributions and density functional theory calculation of TTVPHA. **(J)** Energy levels of S<sub>0</sub>-T<sub>1</sub> and S<sub>1</sub>-T<sub>2</sub> of TTVPHA.

## 2. Cellular uptake of T-T NPs *in vitro*

Confocal laser scanning microscopy (CLSM) was employed for real-time, *in situ* monitoring of T-T NP cell entry in human melanoma A2058 and human hepatocellular carcinoma MHCC 97H cells. As shown in **Figure 2A**, **Figure S3**, strong red fluorescence from T-T NPs was initially observed on the cell membrane of both A2058 and MHCC 97H cells after 10 min of incubation. With continued incubation up to 4 h, red fluorescence increasingly localized in the cytoplasm. This progressive increase in fluorescence intensity corresponded with the concentration of T-T NPs, as confirmed by co-staining with the blue-emissive nuclei dye DAPI and the green-emissive cytoskeleton dye F-actin in **Figures 2B**, **Figure S4-5**. To assess the impact of TAT on T-T NPs uptake, tumor cells were pre-treated with genistein, an TAT inhibitor [36], which significantly reduced T-T NPs internalization, as seen in both CLSM images and flow cytometry (FCM) analysis in **Figure 2C**. Further experiments were conducted to investigate the organelle-targeting capability of T-T NPs through co-staining with LysoTracker Green (LTG) and MitoTracker Green (MTG). As illustrated in **Figure 2D**, red fluorescence from T-T NPs initially showed high co-localization with LTG after 1 h of incubation. However, with additional incubation to 4 h, the co-localization ratio with LTG decreased significantly from 0.88 to 0.51 in A2058 cells and from 0.89 to 0.59 in MHCC 97H cells (**Figure S6**). Concurrently, high Pearson's correlation coefficients of 0.94 and 0.97 with MTG were observed in A2058 and MHCC 97H cells, respectively, indicating strong mitochondrial targeting. These results suggest that TTVPHA gradually escapes from T-T NPs and accumulates in mitochondria, likely due to its positive charge and delocalization properties. This mitochondrial targeting enhances its potential in anticancer therapy and provides a basis for further exploration of the mechanisms through which T-T NPs exert tumor cell damage.



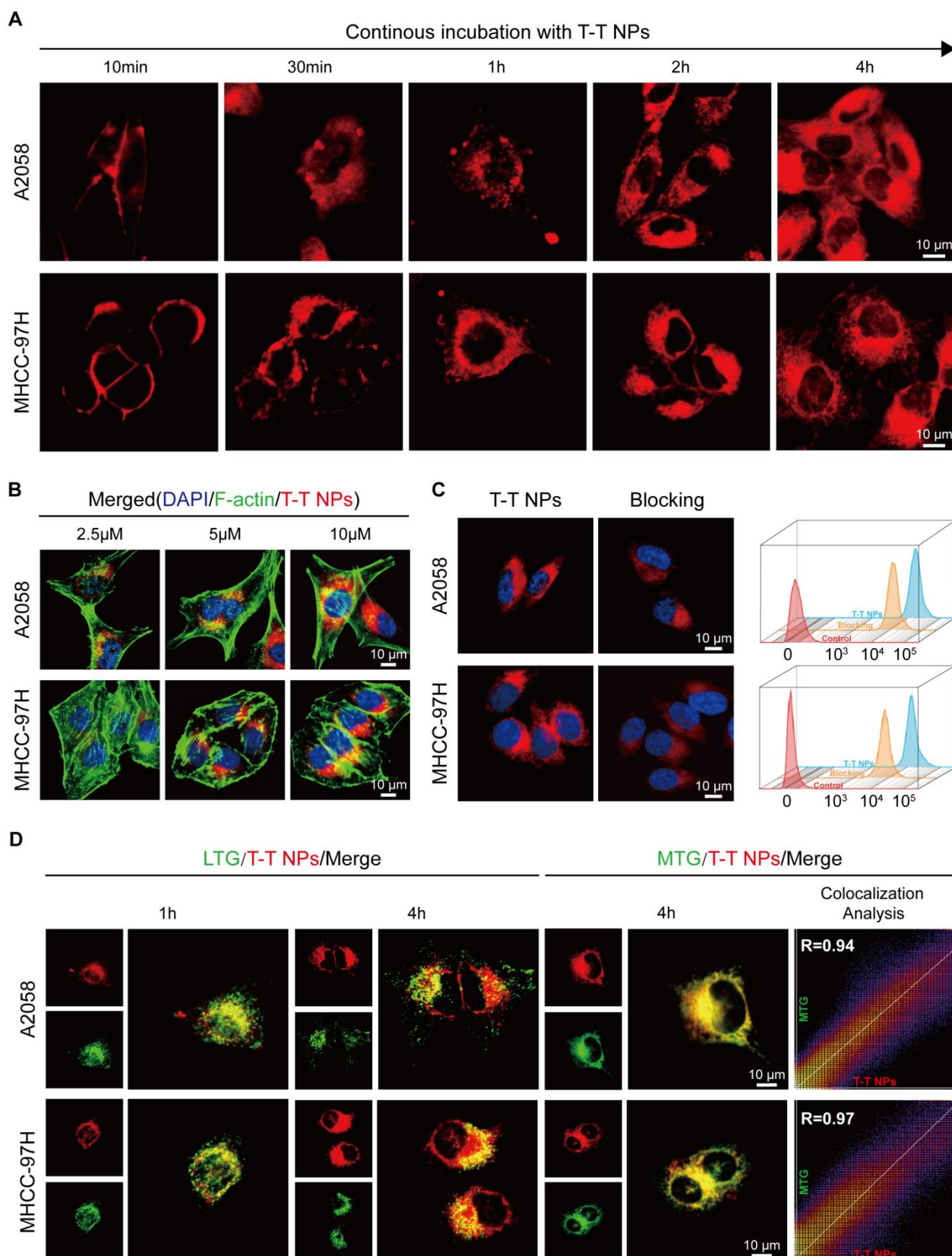


**Figure 2. The cellular uptake and organelle-targeting of T-T NPs in A2058 cells and MHCC 97H cells. (A)** Dynamic fluorescence images of T-T NPs accumulation in cells with different incubation time monitored by confocal laser scanning microscopy (CLSM). **(B)** Cellular uptake of T-T NPs in cells with different concentrations

monitored by CLSM. **(C)** Confocal images and Flow cytometry analysis of cells after incubation with T-T NPs for 4 h. Blocking group was pretreated by genistein for 2 h. **(D)** Co-localization imaging and quantitation analysis of A2058 cells and MHCC 97H cells stained with T-T NPs, LysoTracker Green (LTG) and MitoTracker Green (MTG) observed by CLSM.

### 3. Photodynamic therapeutic performance *in vitro*

After confirming the efficient uptake of T-T NPs by cancer cells and their mitochondria-targeted accumulation of TTVPHA, we evaluated the photodynamic therapeutic efficacy of T-T NPs. In the dark, T-T NPs showed excellent biocompatibility, maintaining cell viability close to 100% even at a high concentration of 10  $\mu$ M TTVPHA under both normoxic (21% O<sub>2</sub>) and hypoxic (1% O<sub>2</sub>) conditions (**Figure 3A, Figure S7**). In contrast, the survival rates of A2058 and MHCC 97H cells incubated with T-T NPs containing 5  $\mu$ M TTVPHA gradually decreased with extended light exposure from 0 to 10 min (**Figure 3B**). For comparison, the control groups with only light or T-T NPs in the dark showed no decrease in cell viability (**Figure 3E**). The robust ROS generation capability of T-T NPs under light irradiation was confirmed by the ROS indicator DCFH-DA under normoxic conditions (**Figure 3C, Figure S8**). Specific ROS fluorescent probes, including DHR123 for O<sub>2</sub><sup>•-</sup> and HPF for •OH, were used to verify TTVPHA's type I photodynamic ability. As shown in **Figure 3D, Figure S9**, under hypoxia, the fluorescence intensities of DHR123 and HPF sharply increased in the presence of T-T NPs upon light exposure, strongly indicating that TTVPHA retains its type I photosensitizer properties in cells, producing ROS independently of oxygen levels—a crucial advantage for enhanced tumor-killing efficacy. Due to TTVPHA's mitochondrial targeting, we further investigated whether PDT-induced ROS could damage mitochondria to enhance tumor cell death. Using the JC-10 probe to indicate mitochondrial membrane potential, the PDT group showed primarily green fluorescence from JC-10 monomers, indicating significant mitochondrial membrane potential depolarization ( $\Delta\psi$ m) compared to other groups (**Figure 3F, Figure S10**). Subsequent live-cell staining with Calcein-AM under identical light conditions revealed that only 20-30% of cells remained viable in the PDT group (**Figure 3G-H**), corroborating the CCK8 assay results. Overall, these findings demonstrate that T-T NPs-mediated PDT generates substantial ROS levels under both normoxic and hypoxic conditions, resulting in mitochondrial damage and potent cytotoxicity against tumor cells. These results underscore the promising therapeutic potential of T-T NPs for anticancer treatment.

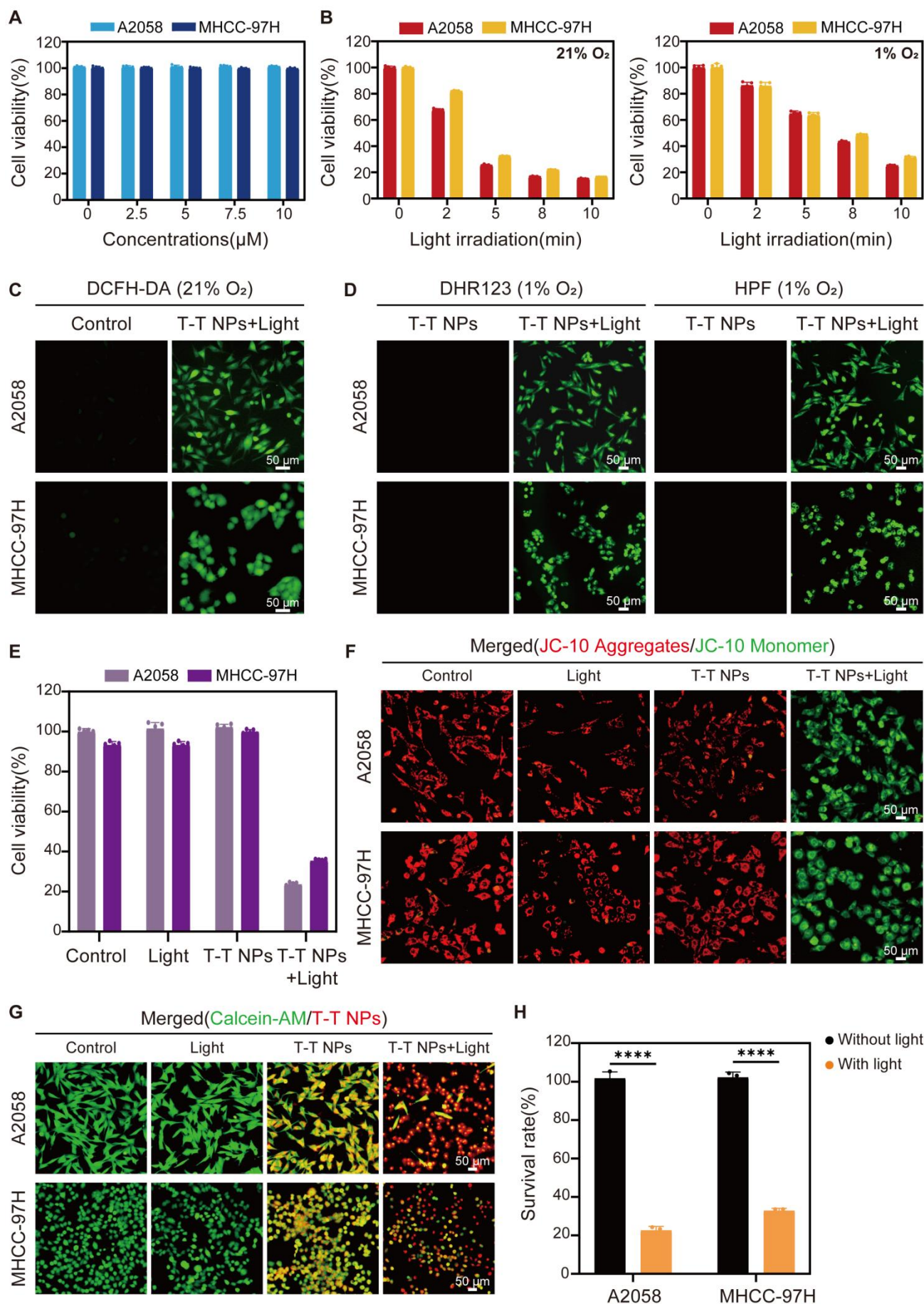


**Figure 3. *In vitro* Photodynamic therapeutic performance of T-T NPs on A2058 and MHCC 97H cells.** (A) Cytotoxicity of A2058 and MHCC 97H cells treated with varying concentrations of T-T NPs without light exposure under normoxic conditions, assessed by CCK8 assay. (B) Time-dependent phototoxicity of T-T NPs under normoxic and hypoxic conditions. (C) Intracellular ROS generation observed by fluorescence microscopy in T-T NPs-treated cells after light exposure, using DCFH-DA (20  $\mu$ M) as a probe under normoxia. (D) Detection of intracellular  $O_2^{\cdot-}$  and  $\cdot OH$  using DHR123 (20  $\mu$ M) and HPF (20  $\mu$ M) indicators in the presence of T-T NPs, with or without light exposure under hypoxia. (E) Cell viability of A2058 and MHCC 97H cells subjected to different treatments, measured by CCK8 assay. (F) Mitochondrial membrane potential ( $\Delta\Psi_m$ ) in A2058 and MHCC 97H cells following various treatments, stained with the JC-10 probe. (G) Fluorescence imaging and (H) quantitative analysis of live cell staining using Calcein-AM (2  $\mu$ M) for A2058 and MHCC 97H cells under different treatments. \*\*\*\* $p < 0.0001$ . Light exposure = 300 mW $\cdot$ cm $^{-2}$ , [TTVPHA] = 5  $\mu$ M.

#### 4. Potential therapeutic mechanism of T-T NPs-mediated PDT

To elucidate the mechanisms underlying T-T NPs-mediated PDT, whole-transcriptome analysis was conducted, identifying 507 and 146 differentially expressed genes (DEGs) ( $|\log_2(\text{Fold Change})| \geq 1$ ,  $q < 0.05$ ) in A2058 and MHCC 97H cells, respectively (**Figure 4B**). Volcano plots depict the upregulated and downregulated genes (**Figure 4A**). Gene Ontology (GO) pathway enrichment analysis of DEGs in both cell lines (**Figure 4C**) revealed significant enrichment in biological processes (BP), with DEGs associated with multiple functions, including negative regulation of cell proliferation and positive regulation of apoptosis and metabolic processes. These DEGs are also linked to protein ubiquitination regulation and pathways such as the JNK/MAPK cascade [37], histone acetylation [38-39], and tyrosine/threonine phosphatase activity [40]. These pathways are known to participate in various cell death mechanisms, including apoptosis, pyroptosis, ferroptosis, and necroptosis. Based on these observations, we hypothesize that PDT with T-T NPs induces multiple cancer cell death pathways. To test this hypothesis, cancer cells were pretreated with inhibitors specific to various cell death pathways before T-T NPs treatment, including Z-VAD-FMK (apoptosis inhibitor), ferrostatin-1 (ferroptosis inhibitor), necrostatin-1 (necroptosis inhibitor), chloroquine (autophagy inhibitor), and 2-bromohexadecanoic acid (pyroptosis inhibitor). All inhibitors increased cell survival and mitigated the therapeutic effects of T-T NPs under light exposure (**Figure 4D**). These findings indicate that mitochondria-targeted PDT can trigger multiple cell death pathways, warranting further investigation into the detailed therapeutic mechanisms.





**Figure 4. Investigation of potential cell death mechanism in T-T NPs-mediated PDT on A2058 and MHCC 97H cells. (A)** Volcano plot of DEGs in A2058 and MHCC 97H cells under control and PDT conditions. **(B)** Histogram of DEG counts in the control versus PDT groups. **(C)** GO pathway enrichment analysis of altered genes in the PDT group compared to the control group. **(D)** Cell viability of A2058 and MHCC 97H cells treated with T-T NPs with or without light exposure in combination with various inhibitors: ferroptosis inhibitor ferrostatin-1 (Fer-1, 50  $\mu$ M), pyroptosis inhibitor 2-bromohexadecanoic acid (2-BP, 5  $\mu$ M), apoptosis inhibitor Z-VAD-FMK (100  $\mu$ M), necroptosis inhibitor necrostatin-1 (Nec-1, 50  $\mu$ M), and autophagy inhibitor chloroquine (CQ, 20  $\mu$ M).

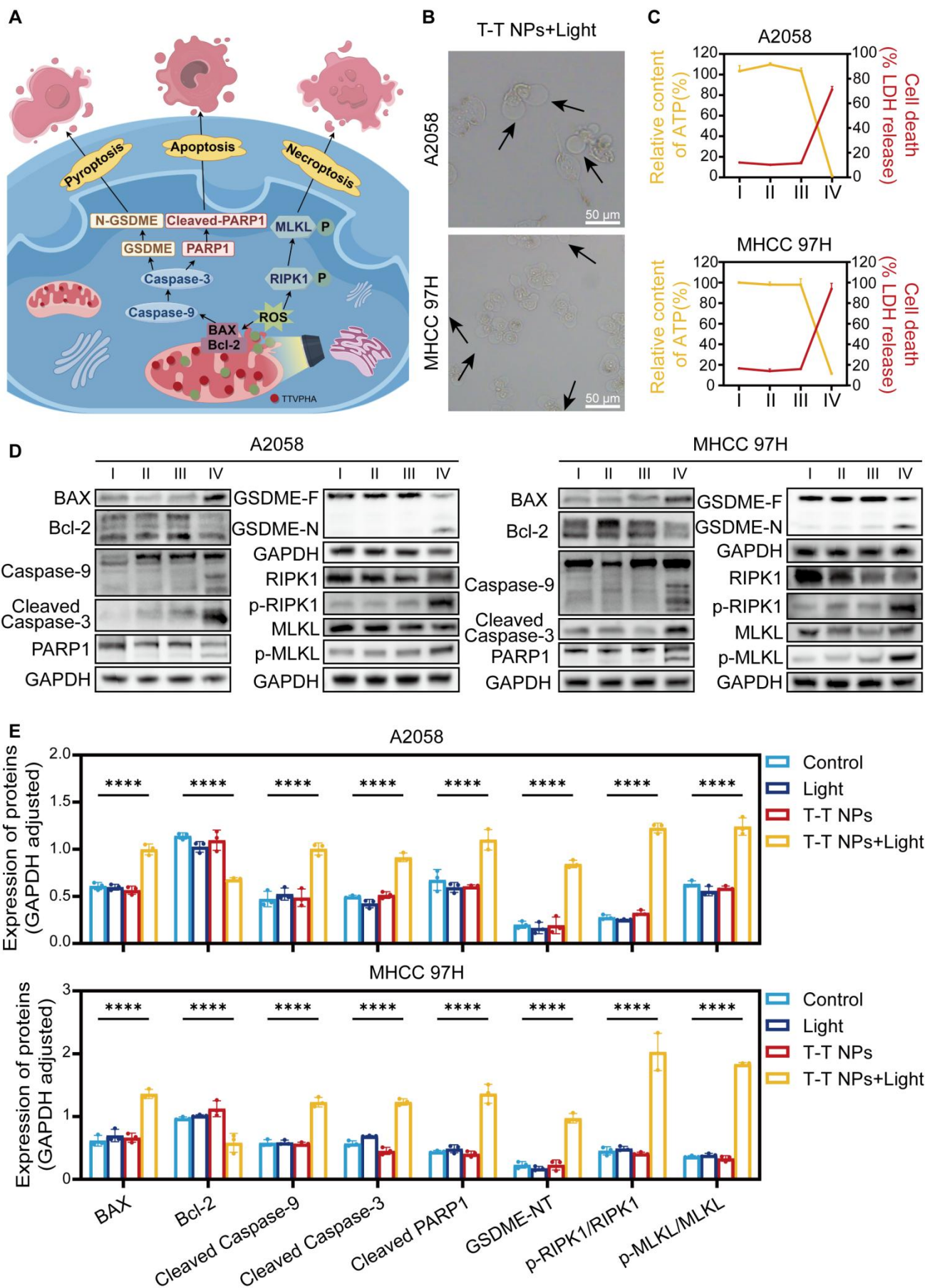
## 5. PANoptosis induced by T-T NPs-mediated PDT

PANoptosis, a form of programmed cell death (PCD), integrates features of apoptosis, necroptosis, and pyroptosis, representing a complex and combined mode of cell death that engages multiple signaling pathways and various effector mechanisms [41-42]. The accumulation of ROS activates several apoptosis-related signaling pathways, including the mitochondrial apoptosis pathway (involving Bcl-2 family proteins), caspase cascades, and transcription factors like p53, all contributing to apoptosis induction. Studies indicate that ROS can downregulate anti-apoptotic proteins (e.g., Bcl-2), triggering apoptosis by activating pro-apoptotic proteins like BAX [43]. Activated BAX disrupts the mitochondrial outer membrane, releasing mitochondrial proteins into the cytosol and activating caspase family proteins to initiate apoptosis [44]. Caspase-9 then cleaves caspase-3, which induces poly (ADP-ribose) polymerase 1 (PARP1) activation, leading to apoptosis [45], and also cleaves gasdermin E (GSDME), releasing the GSDME-N domain and causing vesicle formation, thereby inducing pyroptosis [46]. Additionally, high mitochondrial ROS levels promote receptor-interacting serine/threonine-protein kinase 1 (RIPK1) phosphorylation, which further phosphorylates mixed lineage kinase domain-like pseudokinase (MLKL), ultimately disrupting the plasma membrane, releasing cellular contents, and promoting necroptosis [47]. Based on these pathways, we hypothesize that T-T NPs-mediated PDT could induce PANoptosis in tumor cells, as illustrated in **Figure 5A**.

As shown in **Figure 5B**, **Figure S11**, following PDT treatment, visible membrane bubbling was observed in both A2058 and MHCC 97H cells, a characteristic feature of pyroptosis, while no distinct morphological changes appeared in the other treatment groups. This suggests that T-T NPs-mediated PDT effectively induces pyroptosis. Pyroptotic markers, including lactate dehydrogenase (LDH) and adenosine triphosphate (ATP), were then quantitatively assessed. In the

T-T NPs + Light group, intracellular ATP levels significantly decreased, while extracellular LDH levels increased markedly compared to the control groups (Control, Light, T-T NPs), further indicating pyroptosis induction by T-T NPs-mediated PDT (**Figure 5C**). Western blot analysis (**Figure 5D-E**) revealed key proteins involved in pyroptosis, apoptosis, and necroptosis. In the T-T NPs + Light group, there was a notable decrease in the anti-apoptotic protein Bcl-2, accompanied by a significant upregulation of the pro-apoptotic protein BAX. The increase in BAX led to the activation of caspase-9, confirming the engagement of the intrinsic apoptotic pathway. Cleaved caspase-3, a central executioner in apoptosis, was also detected, indicating the activation of the apoptotic cascade [45]. Caspase-3 cleaves GSDME, generating an N-terminal fragment that forms pores in the plasma membrane, resulting in pyroptosis [46]. The detection of cleaved GSDME in cells treated with PDT supports the simultaneous occurrence of pyroptosis and apoptosis. Additionally, cleaved caspase-3 further activated PARP1, reflecting apoptosis involvement. Phosphorylation of necroptosis-related proteins RIPK1 and MLKL was also observed, validating that necroptosis was triggered by PDT treatment. Altogether, these findings strongly support the induction of PANoptosis by T-T NPs-mediated PDT both in A2058 and MHCC 97H cells, revealing the complex activation of apoptosis, pyroptosis, and necroptosis. This multimodal mechanism offers a potentially comprehensive approach for effectively targeting cancer cells.



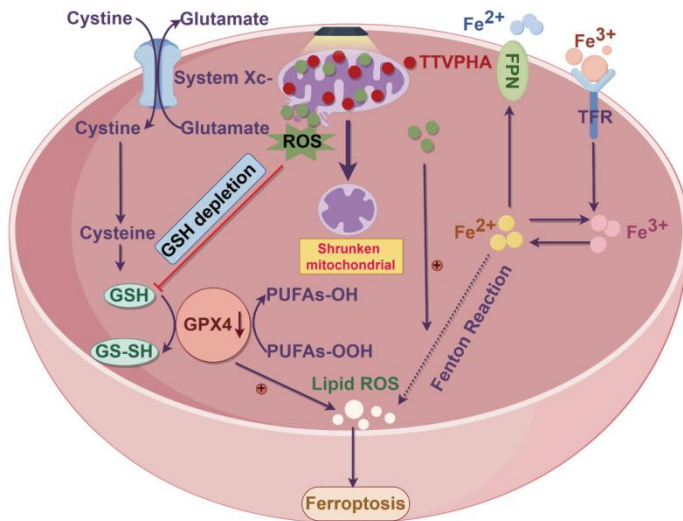
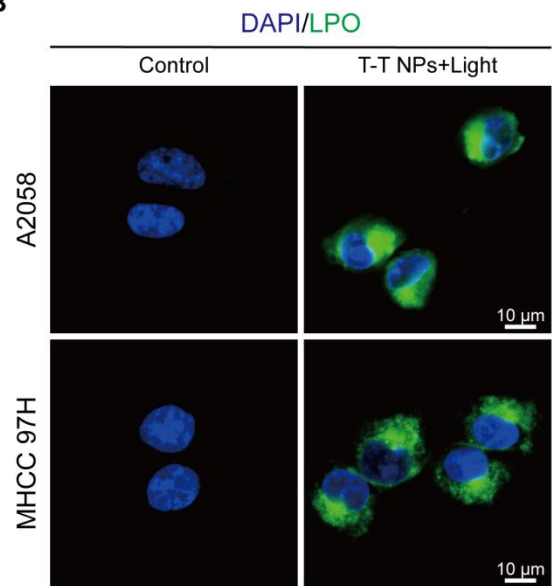
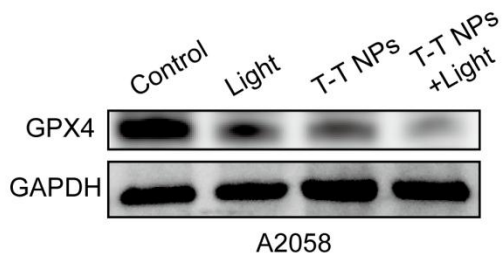
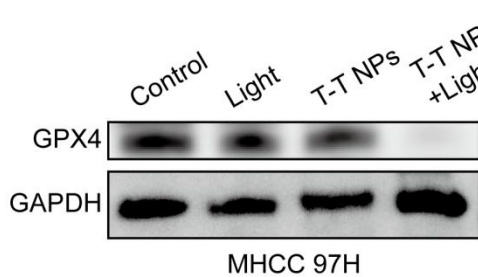
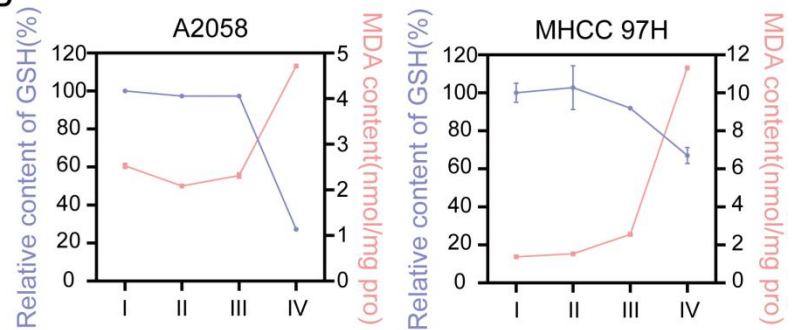
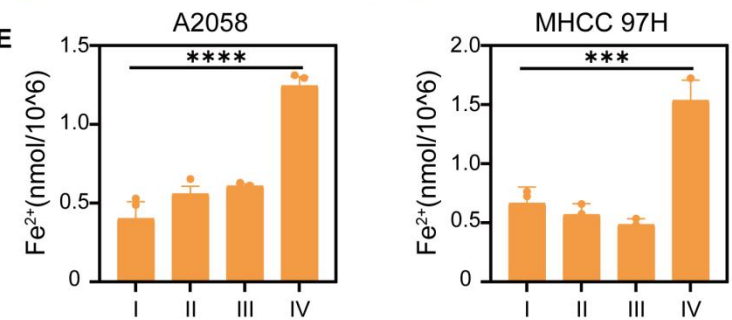
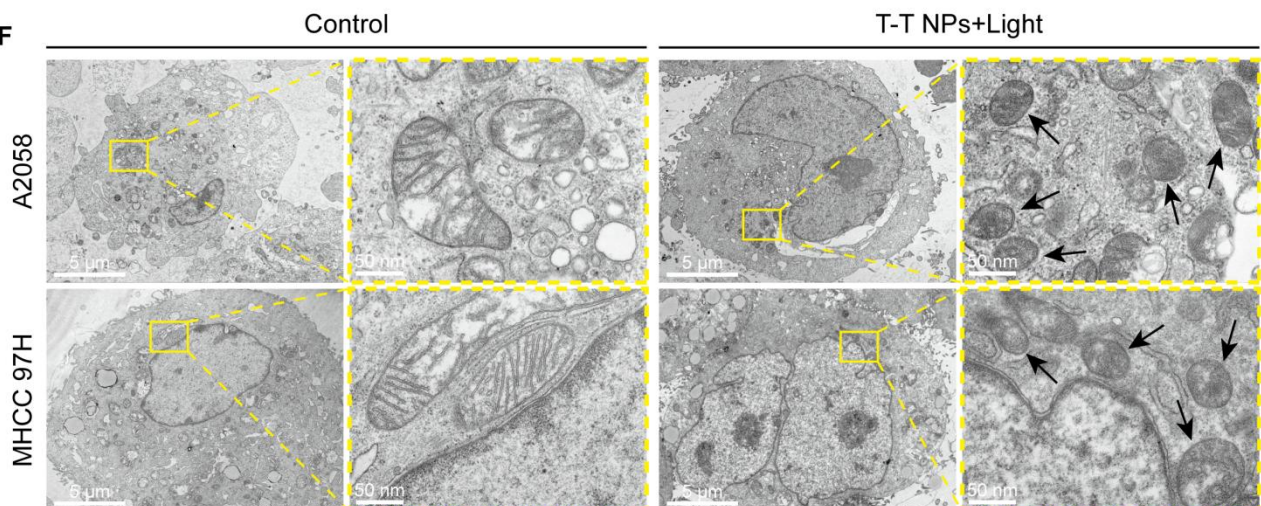


**Figure 5. Characterization of PANoptosis induced by T-T NPs in A2058 and MHCC 97H cells.** (A) Schematic of the PANoptosis mechanism induced by T-T NPs. (B) Representative images showing changes in cell morphology in A2058 and MHCC 97H cells following PDT treatment. (C) Measurement of extracellular lactate dehydrogenase (LDH) and intracellular adenosine triphosphate (ATP) in A2058 and MHCC 97H cells under different treatment conditions. (D) Western blot analysis of key proteins associated with PANoptosis in A2058 and MHCC 97H cells (I: Control, II: Light, III: T-T NPs, IV: T-T NPs + Light). (E) Semi-quantitative analysis of PANoptosis protein expression in A2058 and MHCC 97H cells under different treatments. \*\*\*\* $p < 0.0001$ .

## 6. Ferroptosis induced by T-T NPs-mediated PDT

Ferroptosis is a distinct type of regulated cell death, unlike apoptosis, necrosis, and autophagy. It is marked by iron-dependent lipid peroxide accumulation, ultimately leading to cell death, and is tightly controlled by the balance between pro-oxidation and anti-oxidation processes [48-50]. Excessive ROS production can deplete intracellular glutathione (GSH) and downregulate glutathione peroxidase 4 (GPX4), resulting in lipid peroxidation (LPO) and triggering ferroptosis [14, 51]. ROS can also interact with ferrous iron through the Fenton reaction, generating toxic hydroxyl radicals that further promote LPO and ferroptosis [52]. Thus, we hypothesize that T-T NPs-mediated PDT could induce ferroptosis in tumor cells, as illustrated in **Figure 6A**. Our prior CCK8 results confirmed that the ferroptosis inhibitor ferrostatin-1 (Fer-1) could mitigate the cytotoxic effects of T-T NPs-mediated PDT on A2058 and MHCC 97H cells (**Figure 4D**). LPO, a key biomarker of ferroptosis, was quantified using the fluorescent indicator C11-BODIPY (581/591) dye, and a significantly stronger green fluorescence was observed in the T-T NPs + Light group compared to other groups (**Figure 6B**, **Figure S12**). Additionally, **Figure 6C**, **Figure S13** show markedly reduced expression of GPX4 protein in A2058 and MHCC 97H cells treated with T-T NPs + Light, as revealed by Western blot analysis. Malondialdehyde (MDA), a byproduct of lipid oxidation, serves as an indicator of lipid oxidation under oxidative stress. The elevated MDA levels, along with a substantial reduction in GSH levels and a sharp increase in cellular ferrous iron (**Figures 6D-E**), further support the ability of T-T NPs-mediated PDT to induce strong ferroptosis. Transmission electron microscopy (TEM) was used to examine mitochondrial morphology in cells under different treatments. TEM images revealed that mitochondria in tumor cells treated with T-T NPs + Light displayed classic ferroptotic morphology [48-49], including notable shrinkage and increased mitochondrial membrane density, distinctly different from normal mitochondria (**Figure 6F**).

Collectively, these findings demonstrate that T-T NPs can efficaciously induce ferroptosis in tumor cells through PDT.

**A****B****C****D****E****F**

**Figure 6. Characterization of ferroptosis triggered by T-T NPs in A2058 and MHCC 97H cells.** (A) Schematic representation of the mechanism of ferroptosis induced by T-T NPs. (B) Confocal imaging of lipid peroxidation in A2058 and MHCC 97H cells stained with C11-BODIPY (581/591) dye following PDT with T-T NPs. (C) Western blot analysis of glutathione peroxidase 4 (GPX4) expression in A2058 and MHCC 97H cells under different treatment conditions. (D) Quantification of glutathione (GSH) and malondialdehyde (MDA) levels, and (E) evaluation of Fe<sup>2+</sup> levels in A2058 and MHCC 97H cells across different formulations (I: Control; II: Light; III: T-T NPs; IV: T-T NPs + Light). \*\*\*p < 0.001; \*\*\*\*p < 0.0001. (F) Transmission electron microscopy (TEM) images of mitochondria in A2058 and MHCC 97H cells after PDT with T-T NPs.

## 7. *In vivo* biosafety, tumor imaging and distribution

To evaluate the *in vivo* antitumor potential of T-T NPs-mediated PDT, we first assessed their biosafety and imaging capabilities. Hemocompatibility assays were conducted to evaluate the biocompatibility of T-T NPs for *in vivo* use. As shown in **Figure 7A**, T-T NPs at various concentrations caused no significant hemolysis, similar to the saline-treated negative control group, while distilled water (positive control) led to substantial hemolysis. These results suggest that T-T NPs are hemocompatible and suitable for intravenous administration. For systemic toxicity evaluation, 125  $\mu$ L of T-T NPs (4 mg/mL) or PBS was administered intravenously to two groups of healthy nude mice. Seven days post-injection, blood samples were collected to analyze markers of liver and kidney function, including LDH, Aspartate Aminotransferase (AST), Alanine Aminotransferase (ALT), Blood Urea Nitrogen (BUN), Creatinine (CREA), and Uric Acid (UA). Major organs (heart, liver, spleen, lung, and kidney) were harvested for histological analysis via hematoxylin and eosin (H&E) staining. As shown in **Figure 7B**, no significant differences were observed between the T-T NPs and PBS groups for these markers, and histological analysis (**Figure 7C**) revealed no pathological changes in the T-T NPs group compared to the PBS group. Together, these results indicate that T-T NPs exhibit excellent biosafety, supporting their use in *in vivo* antitumor applications. The biodistribution and tumor-targeted imaging of T-T NPs were assessed using non-invasive fluorescence imaging in an A2058 tumor-bearing mouse model. *In vivo* imaging showed peak fluorescence intensity at 24 h post-injection, suggesting gradual accumulation of T-T NPs in the tumor (**Figure 7D**). To further explore tumor-specific accumulation, *ex vivo* imaging was conducted 24 h post-injection. As shown in **Figures 7D-E**, fluorescence intensity was significantly higher in the tumor compared to major organs, indicating selective accumulation of T-T NPs in



tumor tissue.

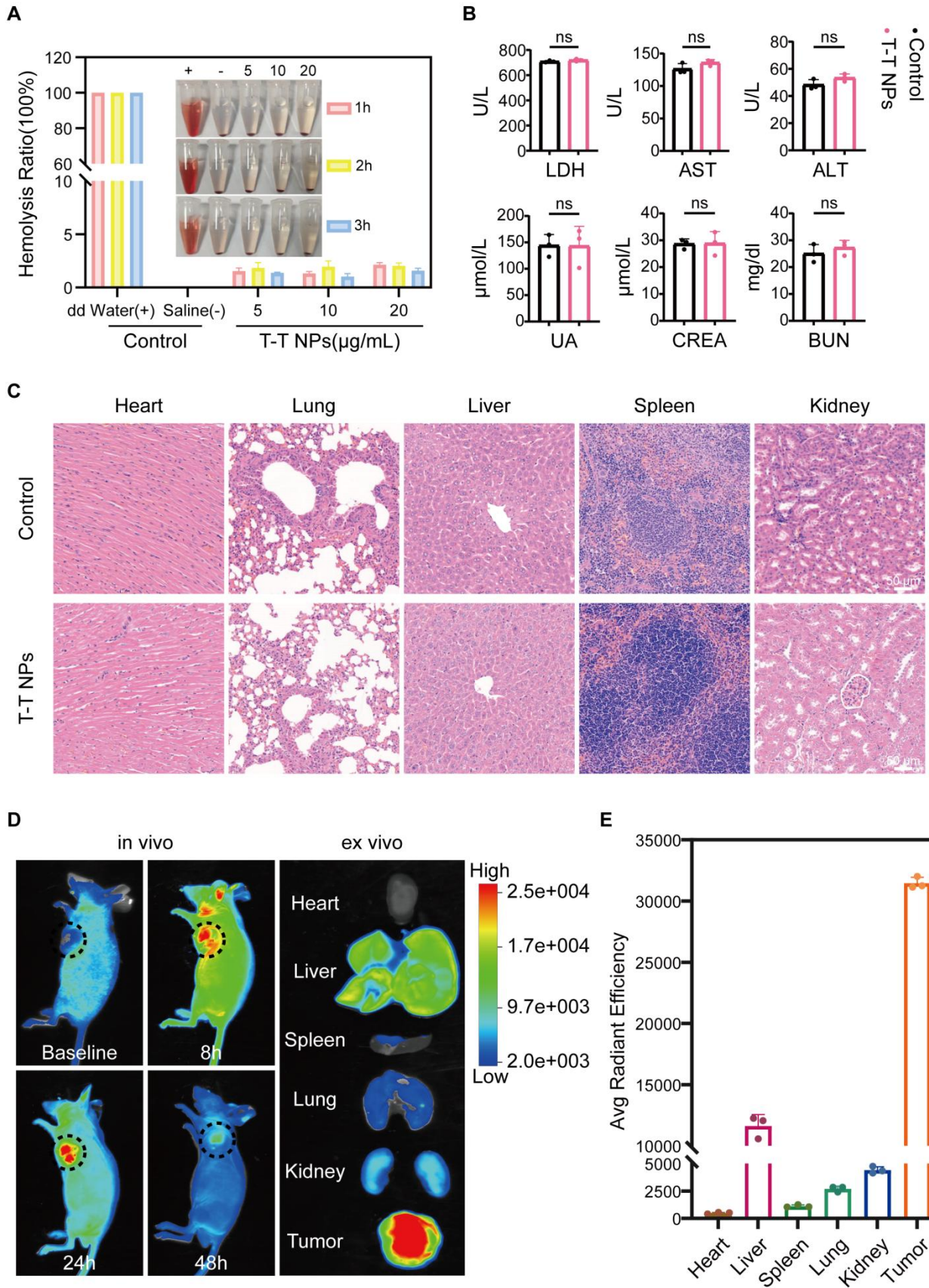


**Figure 7. Biocompatibility and biodistribution of T-T NPs *in vivo*.** (A) Hemolysis assay of mouse red blood cells exposed to T-T NPs at varying concentrations over a set period. Inset: Optical image showing hemolysis extent after sample centrifugation. (B) Blood biochemical analysis for liver function (LDH, AST, ALT) and renal function (UA, CREA, BUN) in mice following intravenous injection of T-T NPs (30 mg/kg). Data are shown as mean  $\pm$  SD (n = 3 per group), with no statistical differences observed (ns). (C) H&E staining of major organs following intravenous injection of T-T NPs (30 mg/kg) for histopathological examination. (D) *In vivo* dynamic fluorescence imaging of A2058 tumor-bearing mice at various time points post-intravenous injection of T-T NPs (30 mg/kg). *Ex vivo* fluorescence imaging of tumors and major organs harvested at 24 h post-injection of T-T NPs (30 mg/kg). (E) Quantitative *ex vivo* analysis of fluorescence in various organs and tumor tissue from mice treated with T-T NPs, 24 h post-injection.

## 8. Anti-tumour effects of T-T NPs-mediated PDT *in vivo*

To assess the antitumor efficacy of T-T NPs-mediated PDT *in vivo*, an A2058 tumor-bearing mouse model was established (**Figure 8A**). As shown in **Figure 8B**, body weight remained stable across all treatment groups, indicating excellent *in vivo* biocompatibility of T-T NPs. Furthermore, PDT-treated mice exhibited obvious tumor growth inhibition compared to other groups (**Figure 8C**). Neither the T-T NPs-only nor the light-only groups showed notable tumor inhibition, similar to the control group treated with PBS. By the end of the treatment period, the relative tumor volume in the PDT group was approximately 20% of the initial size, markedly lower than in other groups (**Figure 8E**). Representative images of treated mice display tumor sizes across different groups (**Figure 8D**). Tumors were excised, weighed, and imaged post-treatment, revealing that the T-T NPs + Light group had significantly smaller tumors and a tumor inhibition rate of approximately 72.5% (**Figures 8F-G**). Histological analyses, including H&E staining, Ki67 immunostaining, and TUNEL assays, were performed on tumor tissues. As shown in **Figure 8H**, the T-T NPs + Light group exhibited extensive nuclear loss, reduced Ki67 expression, and increased apoptosis (**Figure S14**), underscoring the potent antitumor effect of T-T NPs-mediated PDT *in vivo*.

To investigate whether T-T NPs-mediated PDT could induce PANoptosis and ferroptosis *in vivo*, Western blot analysis was conducted on key proteins in tumor tissues (**Figure 8I, Figure S15**). The T-T NPs + Light group showed elevated levels of pro-apoptotic protein BAX and activated caspase-3, confirming notable apoptosis in tumor tissues. The distinct cleavage of GSDME, a pyroptosis marker, suggests that T-T NPs-mediated PDT also induces pyroptosis *in vivo*. Furthermore, phosphorylated



MLKL, a necroptosis marker, indicates necroptosis activation in PDT-treated tumor tissue. The co-occurrence of these cell death forms implies that PDT can induce PANoptosis *in vivo*. The decreased expression of GPX4, a ferroptosis-related protein, further demonstrates successful induction of ferroptosis. These findings collectively validate that T-T NPs-mediated PDT can simultaneously activate PANoptosis and ferroptosis in both *in vitro* and *in vivo* settings.

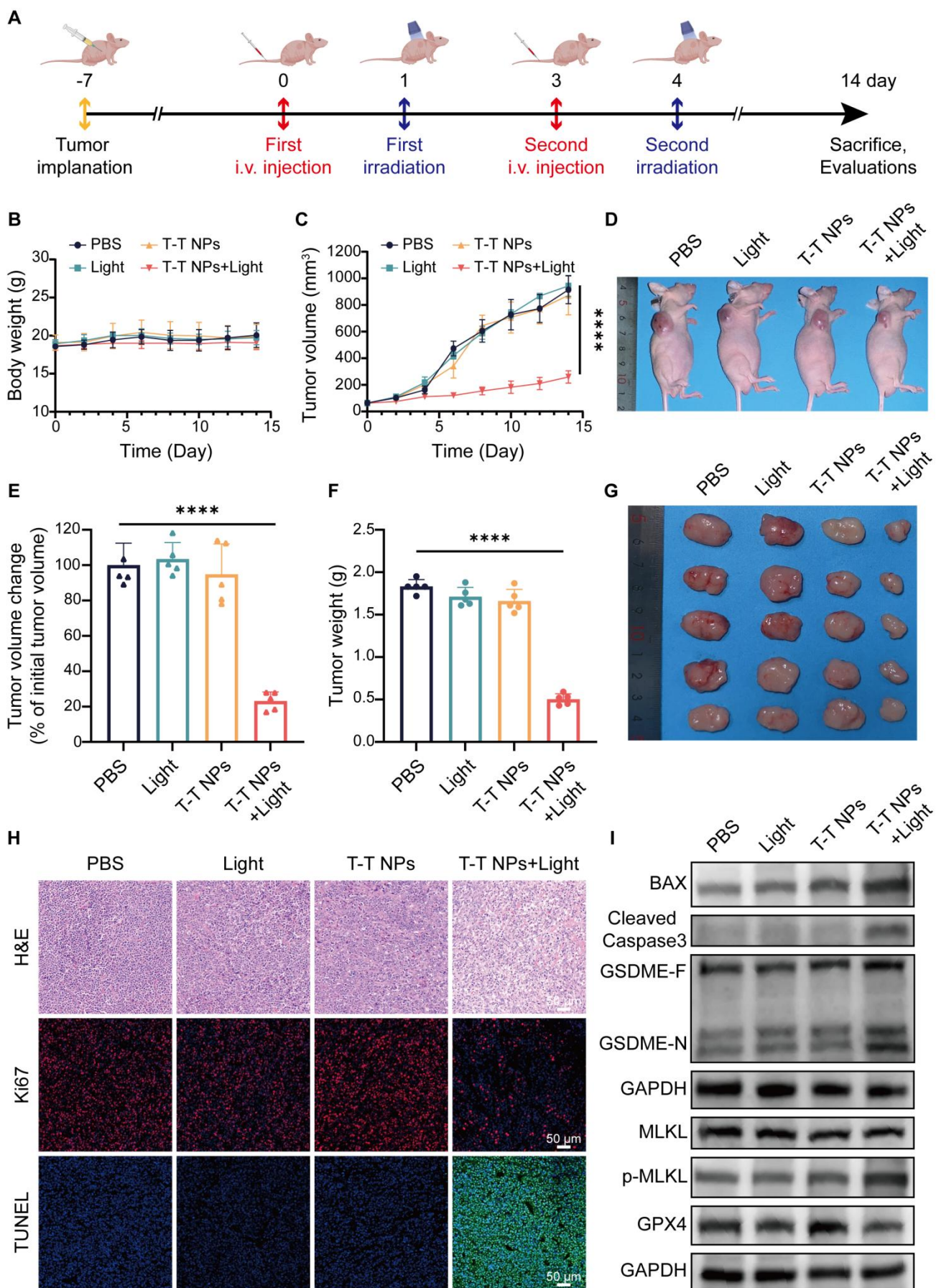


**Figure 8. *In vivo* antitumor efficacy and mechanism of T-T NPs-mediated PDT.** (A) Schematic diagram of the experimental design for *in vivo* tumor therapy (n = 5 per group). (B) Body weight curves of mice over 14 days following different treatments. (C) Tumor volume growth curves, (D) representative photographs, and (E) semi-quantitative analysis of relative tumor volume changes in tumor-bearing mice across treatment groups. (F) Tumor weights and (G) photographs of excised tumors from mice at the end of different treatments. (H) H&E, Ki67, and TUNEL staining of tumor slices on day 14 post-treatment. (I) Western blot analysis of key protein expression in tumor tissue after different treatments. \*\*\*\*p < 0.0001.

## Conclusion

In summary, we successfully developed mitochondria-targeted, AIE-based PS-loaded nanoparticles (T-T NPs) modified with TAT peptides. Extensive *in vitro* and *in vivo* studies demonstrated that T-T NPs-mediated PDT effectively induces both PANoptosis and ferroptosis. This work is the first to establish a therapeutic approach that combines multiple cell death mechanisms—specifically PANoptosis and ferroptosis—within tumor cells, representing a significant advancement in PDT research. By activating a multimodal cell death network, T-T NPs achieve an enhanced antitumor effect, underscoring the potential of this approach to improve therapeutic outcomes. This multimodal strategy not only maximizes tumor cell elimination but also reduces the likelihood of resistance, a frequent obstacle in cancer treatment. The findings here offer critical insights for designing novel PSs and exploring the mechanisms underlying the antitumor effects of PDT. Future research will aim to optimize delivery efficiency and specificity, investigate synergistic combinations, elucidate molecular pathways, and advance clinical translation. By addressing these objectives, this research seeks to propel PDT development and contribute to more effective, personalized cancer treatments. The multimodal cell death network induced by T-T NPs represents a promising new approach in cancer therapy, offering the potential for improved patient outcomes and a deeper understanding of tumor cell death mechanisms.

## References

1. Ma JY, Tai ZG, Li Y, Yang L, Wang JD, Zhou T, et al. Dissolving microneedle-based cascade-activation nanoplatfrom for enhanced photodynamic therapy of skin cancer. *Int J Nanomedicine*. 2024;19:2057-2070.
2. Mattioli EJ, Ulfo L, Marconi A, Pellicioni V, Costantini PE, Marforio TD, et al. Carrying temoporfin with human serum albumin: A new perspective for photodynamic application in head and neck cancer. *Biomolecules*.

2022;13(1):68.

3. Tan WC, Fulljames C, Stone N, Dix AJ, Shepherd N, Roberts DJ, et al. Photodynamic therapy using 5-aminolaevulinic acid for oesophageal adenocarcinoma associated with Barrett's metaplasia. *J Photochem Photobiol B*. 1999;53(1-3):75-80.
4. Zeng W, Mao R, Zhang Z, Chen X. Combination therapies for advanced biliary tract cancer. *J Clin Transl Hepatol*. 2023;11(2):490-501.
5. Sun F, Chen Y, Lam KWK, Du W, Liu Q, Han F, et al. Glutathione-responsive aggregation-induced emission photosensitizers for enhanced photodynamic therapy of lung cancer. *Small*. 2024;20(40):e2401334.
6. Miao Z, Li J, Zeng S, Lv Y, Jia S, Ding D, et al. Endoplasmic reticulum-targeting aie photosensitizers to boost immunogenic cell death for immunotherapy of bladder carcinoma. *ACS Appl Mater Interfaces*. 2024;16(1):245-260.
7. Correia JH, Rodrigues JA, Pimenta S, Dong T, Yang Z. Photodynamic therapy review: Principles, photosensitizers, applications, and future directions. *Pharmaceutics*. 2021;13(9):1332.
8. Liu MX, Cai YT, Wang RJ, Zhu PF, Liu YC, Sun H, et al. Aggregation-induced emission cns-based nanoparticles to alleviate hypoxic liver fibrosis via triggering hsc ferroptosis and enhancing photodynamic therapy. *ACS Appl Mater Interfaces*. 2024;16(26):33021-33037.
9. Chai C, Zhou T, Zhu J, Tang Y, Xiong J, Min X, et al. Multiple light-activated photodynamic therapy of tetraphenylethylene derivative with aie characteristics for hepatocellular carcinoma via dual-organelles targeting. *Pharmaceutics*. 2022;14(2):459.
10. Liu J, Chen W, Zheng C, Hu F, Zhai J, Bai Q, et al. Recent molecular design strategies for efficient photodynamic therapy and its synergistic therapy based on AIE photosensitizers. *Eur J Med Chem*. 2022;244:114843.
11. Kang M, Zhang Z, Song N, Li M, Sun PP, Chen XH, et al. Aggregation-enhanced theranostics: AIE sparkles in biomedical field. *Aggregate*. 2020; 1: 80–106.
12. Cao S, Shao J, Abdelmohsen LKEA, van Hest JCM. Amphiphilic AIEgen-polymer aggregates: Design, self-assembly and biomedical applications. *Aggregate*. 2022;3(1):e128.
13. Sun, ZC, Wang JX, Xiao MH, Wu KY, Wang C, Hao F, et al. A straightforward strategy to modulate ROS generation of AIE photosensitizers for type-I PDT. *Chemical Engineering Journal*. 2024;499:155782.
14. Wang YQ, Xu Y, Qu Y, Jin YF, Cao JM, Zhan JS, et al. Ferroptosis: A novel cell death modality as a synergistic therapeutic strategy with photodynamic therapy. *Photodiagnosis Photodyn Ther*. 2025;51:104463.

15. Gao Y, Zheng QC, Xu S, Yuan Y, Cheng X, Jiang S, et al. Theranostic nanodots with aggregation-induced emission characteristic for targeted and image-guided photodynamic therapy of hepatocellular carcinoma. *Theranostics*. 2019;9(5):1264-1279.
16. Li M, Gao Y, Yuan Y, Wu Y, Song Z, Tang BZ, et al. One-step formulation of targeted aggregation-induced emission dots for image-guided photodynamic therapy of cholangiocarcinoma. *ACS Nano*. 2017;11(4):3922-3932.
17. Tang Y, Zhang Q, Chen H, Chen, G, Li, Z, Chen, G, et al. A integrated molecule based on ferritin nanoplateforms for inducing tumor ferroptosis with the synergistic photo/chemodynamic treatment. *ACS Appl Mater Interfaces*. 2025;17(4):5909-5920.
18. Liu M, Liu Y, Cai Y, Gu Y, Zhu Y, Zhang N, et al. Self-produced O<sub>2</sub> CNS-based nanocarriers of dna hydrophobization strategy triggers photodynamic and mitochondrial-derived ferroptosis for hepatocellular carcinoma combined treatment. *Adv Healthc Mater*. 2024;13(31):e2402110.
19. Zhang B, Wang Y, Wang S, Tang Y, Li Z, Lin Y, et al. Precise RNA editing: cascade self-uncloaking dual-prodrug nanoassemblies based on CRISPR/Cas13a for pleiotropic immunotherapy of PD-L1-resistant colorectal cancer. *Adv Funct Mater*. 2023, 33, 2305630.
20. Wang M, Wu M, Liu X, Shao S, Huang J, Liu B, et al. Pyroptosis remodeling tumor microenvironment to enhance pancreatic cancer immunotherapy driven by membrane anchoring photosensitizer. *Adv Sci (Weinh)*. 2022;9(29):e2202914.
21. Fang L, Meng Q, Wang J, Tu Y, Qu H, Diao Y, et al. Multifunctional single-component photosensitizers as metal-free ferroptosis inducers for enhanced photodynamic immunotherapy. *Acta Biomater*. 2024;186:383-395.
22. Zhu T, Shi L, Yu C, Dong Y, Qiu F, Shen L, et al. Ferroptosis promotes photodynamic therapy: Supramolecular photosensitizer-inducer nanodrug for enhanced cancer treatment. *Theranostics*. 2019;9(11):3293-3307.
23. Liu D, Liang M, Tao Y, Liu H, Liu Q, Bing W, et al. Hypoxia-accelerating pyroptosis nanoinducers for promoting image-guided cancer immunotherapy. *Biomaterials*. 2024;309:122610.
24. Yu B, Liu M, Jiang L, Xu C, Hu H, Huang T, et al. Aggregation-induced emission photosensitizer-engineered anticancer nanomedicine for synergistic chemo/chemodynamic/photodynamic therapy. *Adv Healthc Mater*. 2024;13(11):e2303643.
25. Liu S, Pei Y, Sun Y, Wang Z, Chen H, Zhu D, et al. “Three birds with one stone” nanoplatfrom: Efficient near-infrared-triggered type-I AIE photosensitizer for mitochondria-targeted photodynamic therapy against hypoxic tumors. *Aggregate*. 2024, 5, e547.
26. Zhuang J, Wang B, Chen H, Zhang K, Li N, Zhao N, et al. Efficient NIR-II Type-I AIE photosensitizer for

mitochondria-targeted photodynamic therapy through synergistic apoptosis-ferroptosis. *ACS Nano*. 2023;17(10):9110-9125.

27. Zhang L, Song A, Yang QC, Li SJ, Wang S, Wan SC, et al. Integration of AIEgens into covalent organic frameworks for pyroptosis and ferroptosis primed cancer immunotherapy. *Nat Commun*. 2023;14(1):5355.

28. Cao J, Qu Y, Zhu S, Zhan J, Xu Y, Jin Y, et al. Safe transportation and targeted destruction: Albumin encapsulated aggregation-induced emission photosensitizer nanoaggregate for tumor photodynamic therapy through mitochondria damage-triggered pyroptosis. *Aggregate*. 2024:e637.

29. Li S, Chen Y, He P, Ma Y, Cai Y, Hou X, et al. Aggregation-Induced Emission (AIE) photosensitizer combined polydopamine nanomaterials for organelle-targeting photodynamic and photothermal therapy by the recognition of sialic acid. *Adv Healthc Mater*. 2022;11(15):e2200242.

30. Zhou T, Zhu J, Shang D, Chai C, Li Y, Sun H, et al. Mitochondria-anchoring and AIE-active photosensitizer for self-monitored cholangiocarcinoma therapy. *Mater Chem Front*. 2020;4, 3201-3208.

31. Wang J, Hou Q, Qu J, Huo X, Li H, Feng Y, et al. Polyhedral magnetic nanoparticles induce apoptosis in gastric cancer stem cells and suppressing tumor growth through magnetic force generation. *J Control Release*. 2024;373:370-384.

32. Kim B, Song JH, Lee M. Combination of TAT-HMGB1A and R3V6 amphiphilic peptide for plasmid DNA delivery with anti-inflammatory effect. *J Drug Target*. 2014;22(8):739-747.

33. Navaridas R, Vidal-Sabanés M, Ruiz-Mitjana A, Altés G, Perramon-Güell A, Yeramian A, et al. In vivo intra-uterine delivery of tat-fused cre recombinase and CRISPR/Cas9 editing system in mice unveil histopathology of pten/p53-deficient endometrial cancers. *Adv Sci (Weinh)*. 2023;10(32):e2303134.

34. Kravchenko SV, Domnin PA, Grishin SY, Vershinin NA, Gurina EV, Zakharova AA, et al. Enhancing the antimicrobial properties of peptides through cell-penetrating peptide conjugation: a comprehensive assessment. *Int J Mol Sci*. 2023;24(23):16723.

35. Nguyen VN, Yan Y, Zhao J, Yoon J. Heavy-atom-free photosensitizers: From molecular design to applications in the photodynamic therapy of cancer. *Acc Chem Res*. 2021;54(1):207-220.

36. Lee EO, Kim SE, Park HK, Kang JL, Chong YH. Extracellular HIV-1 Tat upregulates TNF- $\alpha$  dependent MCP-1/CCL2 production via activation of ERK1/2 pathway in rat hippocampal slice cultures: inhibition by resveratrol, a polyphenolic phytoestrogen. *Exp Neurol*. 2011;229(2):399-408.

37. Pham CG, Papa S, Bubici C, Zazzeroni F, Franzoso G. Oxygen JNKs: phosphatases overdose on ROS. *Dev Cell*. 2005;8(4):452-454.

38. Chen C, Wang J, Zhang S, Zhu X, Hu J, Liu C, et al. Epigenetic regulation of diverse regulated cell death modalities in cardiovascular disease: Insights into necroptosis, pyroptosis, ferroptosis, and cuproptosis. *Redox Biol.* 2024;76:103321.
39. Wang F, Jin Y, Wang M, Luo HY, Fang WJ, Wang YN, et al. Combined anti-PD-1, HDAC inhibitor and anti-VEGF for MSS/pMMR colorectal cancer: a randomized phase 2 trial. *Nat Med.* 2024;30(4):1035-1043.
40. Zheng L, Chen Z, Kawakami M, Chen Y, Roszik J, Mustachio LM, et al. Tyrosine threonine kinase inhibition eliminates lung cancers by augmenting apoptosis and polyploidy. *Mol Cancer Ther.* 2019;18(10):1775-1786.
41. Yang F, Zhang G, An N, Dai Q, Cho W, Shang H, et al. Interplay of ferroptosis, cuproptosis, and PANoptosis in cancer treatment-induced cardiotoxicity: Mechanisms and therapeutic implications. *Semin Cancer Biol.* 2024;106-107:106-122.
42. Ocansey DKW, Qian F, Cai P, Ocansey S, Amoah S, Qian Y, et al. Current evidence and therapeutic implication of PANoptosis in cancer. *Theranostics.* 2024;14(2):640-661.
43. Ortega E, Zamora A, Basu U, Lippmann P, Rodríguez V, Janiak C, et al. An Erlotinib gold(I) conjugate for combating triple-negative breast cancer. *J Inorg Biochem.* 2020;203:110910.
44. Kokoulin MS, Kuzmich AS, Filshtein AP, Prassolov VS, Romanenko LA. Capsular polysaccharide from the marine bacterium *Cobetia marina* induces apoptosis via both caspase-dependent and mitochondria-mediated pathways in HL-60 cells. *Carbohydr Polym.* 2025;347:122791.
45. Goswami P, Singh V, Koch B. Mitochondria mediated inhibitory effect of *Nyctanthes arbor-tristis* (L.) flower extract against breast adenocarcinoma and T-cell lymphoma: An in vitro and in vivo study. *J Ethnopharmacol.* 2024;334:118537.
46. Xiao B, Shi X, Xu X, Liu J, Pan Y, Xu H, et al. In situ formed reactive oxygen species-responsive dipyrindamole prodrug hydrogel: Spatiotemporal drug delivery for chemoimmunotherapy. *J Control Release.* 2024;375:454-466.
47. Lin JF, Hu PS, Wang YY, Tan YT, Yu K, Liao K, et al. Phosphorylated NFS1 weakens oxaliplatin-based chemosensitivity of colorectal cancer by preventing PANoptosis. *Signal Transduct Target Ther.* 2022;7(1):54.
48. Xie Y, Hou W, Song X, Yu Y, Huang J, Sun X, et al. Ferroptosis: process and function. *Cell Death Differ.* 2016;23(3):369-379.
49. Dixon SJ, Lemberg KM, Lamprecht MR, Skouta R, Zaitsev EM, Gleason CE, et al. Ferroptosis: an iron-dependent form of nonapoptotic cell death. *Cell.* 2012;149(5):1060-1072.
50. Jaeschke H, Ramachandran A. Ferroptosis and intrinsic drug-induced liver injury by acetaminophen and other



drugs: A critical evaluation and historical perspective. *J Clin Transl Hepatol*. 2024;12(12):1057-1066.

51. Yang WS, Stockwell BR. Ferroptosis: Death by lipid peroxidation. *Trends Cell Biol*. 2016;26(3):165-176.

52. Zhang G, Chang L, Xu X, He L, Wu D, Wei H, et al. Ultrasmall iridium-encapsulated porphyrin metal-organic frameworks for enhanced photodynamic/catalytic therapy by producing reactive oxygen species storm. *J Colloid Interface Sci*. 2025;677(Pt B):1022-1033.